Check for updates

Amplified piezoelectrically actuated on-chip flow switching for a rapid and stable microfluidic fluorescence activated cell sorter†

Kunpeng Cai, [ID] * Shruti Mankar, Anastasia Maslova, [ID] Taiga Ajiri and Tasuku Yotoriyama

With the potential to avoid cross-contamination, eliminate bio-aerosols, and minimize device footprints, microfluidic fluorescence-activated cell sorting (μ-FACS) devices could become the platform for the next generation cell sorter. Here, we report an on-chip flow switching based μ-FACS mechanism with piezoelectric actuation as a fast and robust sorting solution. A microfluidic chip with bifurcate configuration and displacement amplified piezoelectric microvalves has been developed to build the μ-FACS system. Rare fluorescent microparticles of different sizes have been significantly enriched from a purity of ~0.5% to more than 90%. An enrichment of 150-fold from ~0.6% to ~91% has also been confirmed for fluorescently labeled MCF-7 breast cancer cells from Jurkat cells, while viability after sorting was maintained. Taking advantage of its simple structure, low cost, fast response, and reliable flow regulation, the proposed μ-FACS system delivers a new option that can meet the requirements of sorting performance, target selectivity, device lifetime, and cost-effectiveness of implementation.

1 Introduction

Purification and enrichment of well-defined cell populations from a heterogeneous complex mixture is becoming a critical task in areas of biology and medicine.[1] The need for sorting rare cell populations is rapidly expanding, such as the enrichment of circulating tumor cells (CTCs),[2] circulating fetal cells (CFCs),[3] gene edited mammalian cells,[4] hematopoietic stem cells (HSCs)[5,6] and induced pluripotent stem cells from HSCs.[7] Recently, the demand for high performance cell sorting has been further driven by theranostics and personalized medicine, where treatments are tailored to the prognosis of patients.[8]

Offering numerous advantages over conventional FACS systems, μ-FACS devices could become the next generation cell sorters by reducing device footprints, eliminating bio-aerosols, and simplifying protocols.[1,9–17] Unique approaches, including electric,[18–21] magnetic,[22,23] acoustic,[9,24–34] pneumatic,[35,36] piezo-electric,[37–40] and thermal actuations,[41–43] have been developed as actuation mechanisms for μ-FACS systems.[44] Among them, due to the reliable flow regulation on the microscale, mechanical valving is considered to be one of the promising sorting technologies.[45] A plurality of piezoelectric microvalves have been proposed as high-performance mechanical microvalves,[46–49] displaying the advantages of large driving force, rapid response

Central Research Laboratories, Sysmex Corporation, 4-4-4 Takatsukadai, Nishi-ku, Kobe 651-2271, Japan. E-mail: Cai.Kunpeng@sysmex.co.jp

† Electronic supplementary information (ESI) available. See DOI: 10.1039/d0ra04919k

and high tolerance. The shortcoming of small strokes of piezoelectric microvalves has also been overcome by the hydraulic amplification.[50] However, problems such as complex structure, high cost and leakage are still existing and preventing piezoelectric microvalves from being applied in μ-FACS systems.[51]

In this work, we demonstrate a new design of amplified piezoelectrically actuated microvalve and applied it to demonstrate an on-chip flow switching based sorting mechanism. A bifurcately configured microfluidic chip and displacement amplifiers for piezoelectric actuators have been developed for the construction of the μ-FACS system. A throughput of ~1800 events per second (eps) has been achieved as a proof-of-concept. Using the as-constructed μ-FACS system, rare fluorescent particles at diverse sizes have been significantly enriched from a purity of ~0.5% to more than 90%. The μ-FACS system has also been applied to enrich 0.6% of fluorescently labeled MCF-7 breast cancer cells from Jurkat cells by 150-fold to a purity of ~91%. With the characteristics of simple structure, fast response, low cost, and high reliability, our proposed system provides a new μ-FACS option that can meet the requirements of sorting performance, target selectivity, device lifetime, and cost-effectiveness of implementation.

2 Working principle and theory

2.1 Flow control by piezoelectrically actuated microvalves

The simplified schematic of the microfluidic sorter, including a bifurcated microchannel configuration and amplified

piezoelectrically actuated on-chip microvalves, is shown in Fig. 1(a). Piezoelectric actuators are housed in displacement amplifiers, which are composed of fixed parts and travel parts. The displacement amplifier is mounted in a way that the moving direction of its travel part is perpendicular to the microfluidic channel inside a dimethylpolysiloxane (PDMS) layer. An adapter was applied between the piezoelectric actuator and displacement amplifier to protect the piezoelectric actuator and prolong its lifetime. As shown in Fig. 1(b), the principle of leverage was used to augment a displacement input of the piezoelectric actuator to a displacement of the travel part of the amplifier. The following equation could be used for calibration.

$$d_2 = d_1 \frac{l_2}{l_1} \tag{1}$$

where d_1 is the displacement of the piezoelectric actuator, d_2 is the displacement of the travel part. l_1 and l_2 are the distance from the piezoelectric actuator or travel part to the fulcrum of the lever. As shown in Fig. 1(c), the travel part is adjusted to be tangent to the surface of the PDMS layer. According to the status of driving voltage, the piezoelectric actuator could be alternately tuned between a contraction state and an extension state. When the driving voltage is off, the piezoelectric actuator behaves in a contraction state. Thus, the travel part of the displacement amplifier does not interfere with the microchannel, keeping it as open. Contrarily, when the driving voltage is on, the piezoelectric actuator will act in an extension state, pushing the travel part of the displacement amplifier towards the microchannel

and increase its flow resistance. If l_2 is designed to be much longer than l_1, the microchannel in the PDMS layer could be completely closed. The integration of displacement amplifiers with piezoelectric actuators takes advantage of the fast response of piezoelectric actuators while overcoming its limitation in travel distance. Hence, a rapid and stable on-chip microvalve could be built, which was adapted as the essential component for flow switching of our microfluidic on-chip sorter.

The design of the microfluidic sorting chip is given in Fig. 2(a), while the positioning of travel parts of displacement amplifiers on microfluidic channels are shown in a cross-section view in Fig. 2(b). The sample solution that is introduced into the microfluidic chip will be focused by the sheath fluid at a sample focusing site, as shown in Fig. 2(c). A detection spot is designed along the mainstream to collect signals. A bifurcated sorting site is designed on the downstream to isolate particles in a mixture into separated channels, namely sample channel and waste channel. Travel parts of the two displacement amplifiers, as given in Fig. 2(b), are placed at on-chip valve sites on the downstream to independently regulate the Open–Close status of each microchannel. The stroking area of the travel part of the displacement amplifier onto microchannel is marked in a green dotted circle at location 3 of Fig. 2(c). The width of the microchannel on the downstream of the stroking area is designed to be twice the width of the microchannel on the upstream to reduce backflow when the travel part closes the microchannel. The separated particles could be collected from downstream outlets after sorting.
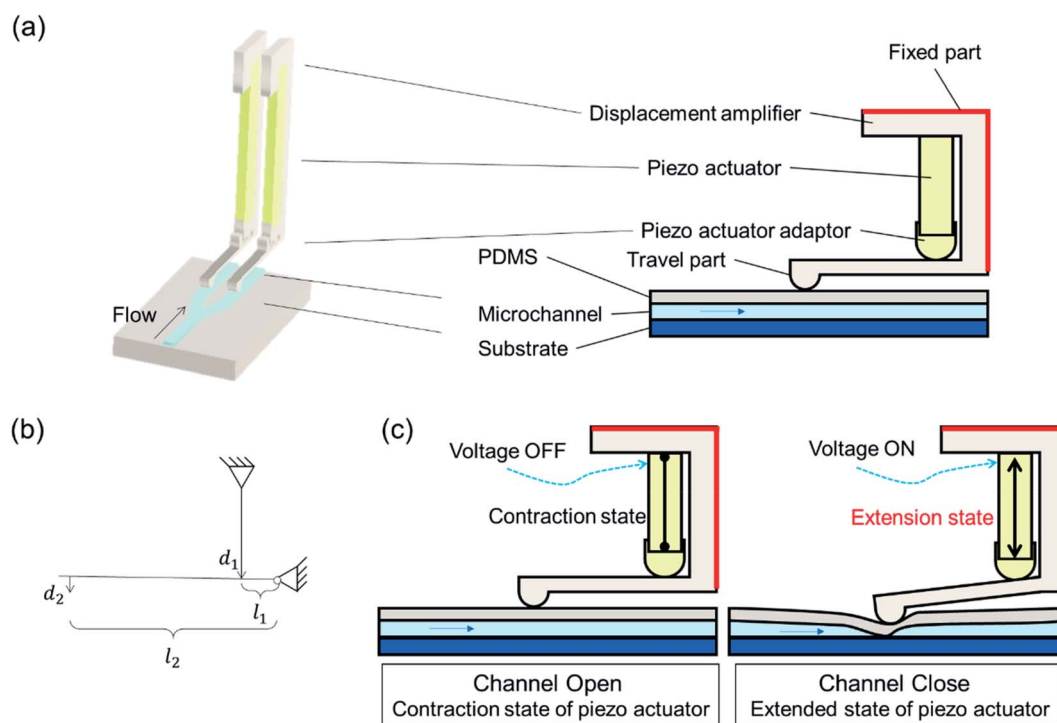

Fig. 1 (a) Schematic of the displacement amplifier and microfluidic sorting mechanism based on on-chip piezoelectric actuator valves. (b) Displacement analysis diagram of the piezoelectric actuator amplifiers. (c) The two interval states of piezoelectric actuators, namely contraction state and extension state, are implied to open and close microchannel respectively.
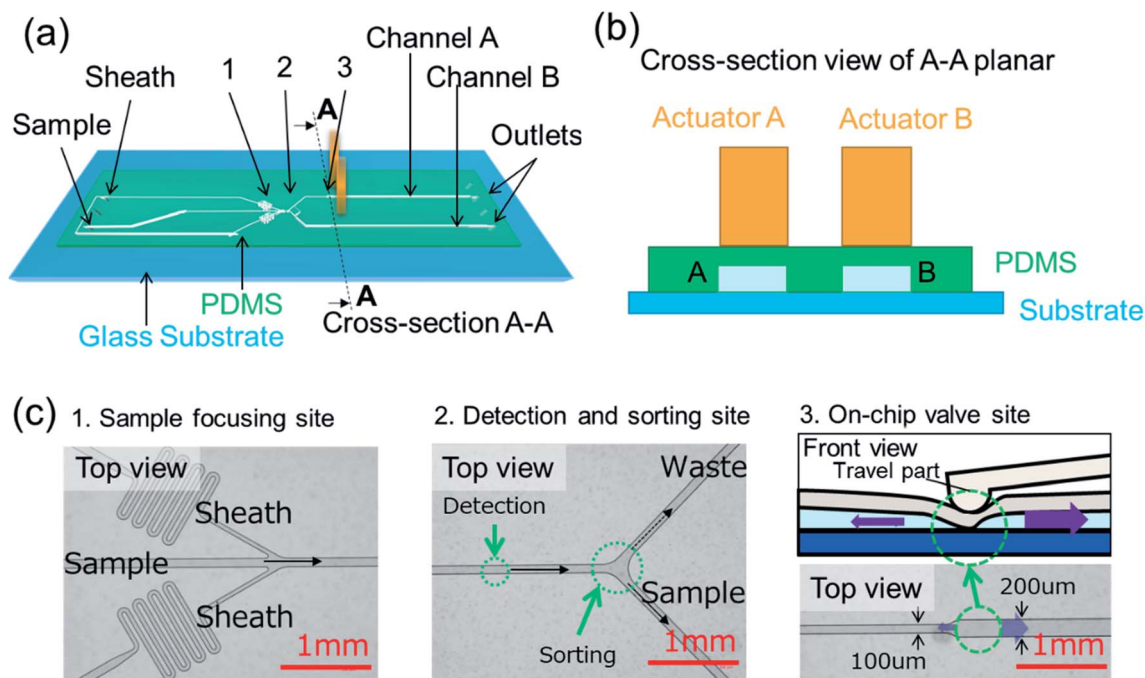
Fig. 2 (a) Design of the microfluidic sorting chip. (b) Cross-section view of the microfluidic chip and piezoelectric actuators. (c) Photos of the microfluidic chip at location 1, 2 and 3 of Fig. 2(a).

2.2 Sorting mechanism of flow switching

Fig. 3 shows an illustration of flow switching during a sorting action. The input voltage on the piezoelectric actuator for the sample channel (B) is kept as normal-on to keep the sample channel as normally closed, as shown in Fig. 3(b). Correspondingly, input voltage on the waste channel (A) is kept as normal-off to maintain the waste channel as normal-open and collect the non-target particles. When a target particle passes through the detection spot, a peak signal would be detected, as shown in Fig. 3(a). If the intensity of the signal exceeds a customer determined threshold, trigger signals would be simultaneously generated to switch the status of voltages on the two piezoelectric actuators and maintain for a user-determined sorting period. During the sorting period, the sample channel (B) will be open, while the waste channel (A) will be closed. As a result, the detected target particle would be collected into the sample channel (B), as shown in Fig. 3(c). After the sorting period, the voltage inputs on piezoelectric actuators would be reset to initial status to shift the successive flow back to the waste channel again.

As shown in Fig. 3(a), the sorting period for a piezoelectric actuator valve could be determined by the following equation,

$$t_{sort} = \frac{t_{rise} - t_{tri}}{2} + (t_{load} - t_{rise}) + \frac{t_{dec} - t_{load}}{2} = t_{load} - t_{tri} \quad (2)$$

where t_{tri}, t_{rise}, t_{load} and t_{dec} are, respectively the moment when the signal is detected to be higher than the threshold, the moment when the voltage on actuator A reaches maximal value V_{max}, the moment when voltage loading on actuator A ends, and the moment when voltage loading on actuator A returns to 0 V.

The volume of liquid that is streamed into the sample channel during the sorting period, namely switching volume, could be defined as follows,

$$v_{swt} = t_{sort} \cdot Q_{samp} \quad (3)$$

where Q_{samp} is the sample flow rate. The theoretical purity after sorting could be calculated by,

$$P_{the} = \frac{N_{target}}{N_{all}} \quad (4)$$

where N_{target} and N_{all} are the number of target particles and the number of total particles collected in v_{swt}, respectively. Giving the concentration of total beads, N_{all} could be further calculated based on Poisson distribution.

3 Experimental

3.1 Manufacturing of microfluidic sorting chip

A two-layer microfluidic sorting chip was implemented for experiments, as shown in Fig. 2. Microfluidic channels with a depth of 40 µm were fabricated in a PDMS layer, the thickness of which is designed as 300 µm. The as-fabricated PMDS layer was then bonded onto a 1 mm thick rigid glass layer. Through holes were opened on the glass layer as inlets and outlets of microfluidic channels. The sorting chip was designed inhouse, while fabrication was outsourced to a domestic semiconductor manufacturer, where standard micro-electromechanical systems (MEMS) fabrication was carried out. A customized fluidics interface was also fabricated to accommodate the microfluidic sorting chip and to improve the user-friendship of sample handling (see ESI files† for more information).
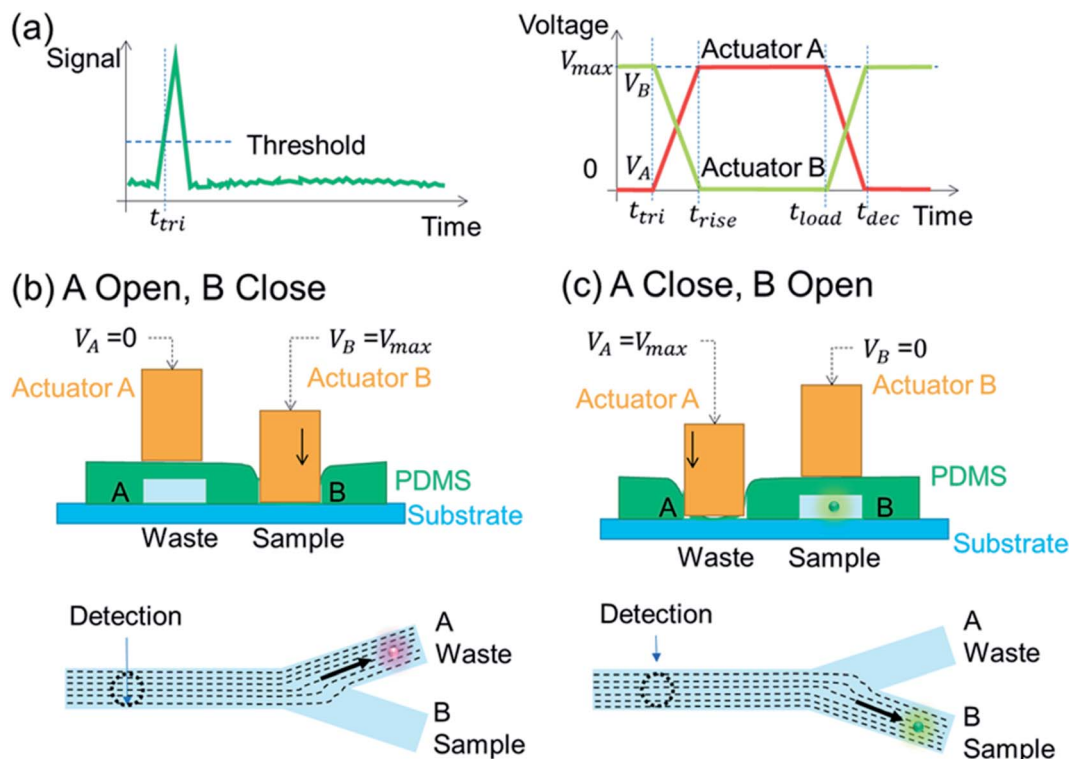
Fig. 3 Illustration of flow switching during sorting. (a) Detection of a typical signal from a particle and corresponding waveforms of the voltage applied on the piezoelectric actuators. (b) The particle is sorted into the waste channel (A), when waste channel (A) is open, while sample channel (B) is closed. (c) The particle is sorted into the sample channel (B), when waste channel (A) is closed, while sample channel (B) is open.

3.2 System of the microfluidic fluorescence-activated sorter

The as-constructed μ-FACS system is shown in Fig. 4(a). An inverted microscope was built to collect signals from the detection spot of the microfluidic sorting chip, which is mounted on the focal plane of an objective lens (PAL-5, Sigmakoki co.,ltd., Japan). A 488 nm and 100 mW laser (OBIS Galaxy Laser Beam Combiner, Coherent, CA, US) was adopted as a light source for excitation. The laser beam was reflected by a long-pass dichroic mirror (DMLP505R, Sigmakoki co.,ltd., Japan) into an objective lens to focus on the detection spot. The excited fluorescent emission signals from samples were then collected into optical lines through the same objective lens. After passing through the DMLP505R long-pass dichroic mirror, 20% of the emission light was split by an ND filter (ND501B, Thorlabs, Inc., US) to a highspeed camera (CHU30-B, Shodensha, Japan) for real-time observation in bright field. After passing through a long-pass dichroic mirror (DMLP550R, Sigmakoki co.,ltd., Japan) and a light filter (MF525-39, Sigmakoki co.,ltd., Japan), the left emission light was focused onto the detection surface of an MPPC module (C13366-1350GA, Hamamatsu Photonics K.K., Japan) for intensity detection of green fluorescence, as shown in Fig. 4(a).

To enable real-time monitoring and control, a high-performance controller (cRIO-9040, National Instruments Corp., US) was applied, with a combination of a data acquisition unit (NI9220, National Instruments Corp., US) and a digital output unit (NI9474, National Instruments Corp., US). A customized control

software interface was correspondingly built using Labview (NI, US). A DC power supply of 3 V was used as the input for the NI9474 unit. To drive the piezoelectric actuators (AE0203D44H40DF, Tokin Corp., Japan), two high-voltage power amplifiers (MTAD3001, Mechano Transformer Corp., Japan) were used to amplify the output voltage of NI9474 from 3 V to 150 V. Fig. 4(b) shows a photo of the as-constructed on-chip microfluidic sorter, which is composed of a sorting chip, piezoelectrically actuated on-chip microvalves, fluidics interface, and optical detection system. Travel parts of the customized displacement amplifiers are positioned towards the PDMS layer, while fixed parts of displacement amplifiers are firmly settled on the fluidics interface.

3.3 Cell culture

MCF-7 (breast cancer cell) was purchased from the American Type Culture Collection (ATCC Cat. no. HTB-22) and cultured in Dulbecco's modified Eagle's medium (DMEM, MilliporeSigma, US) with 10% fetal bovine serum (FBS, MilliporeSigma, US) and 1% antibiotic antimycotic solution (MilliporeSigma, US).

Jurkat cells (T lymphocyte) was purchased from the American Type Culture Collection (ATCC Cat. no. TIB-152) and cultured in RPMI 1640 medium (Thermo Scientific, US) with 10% fetal bovine serum (FBS, MilliporeSigma, US) and 1% antibiotic antimycotic solution (MilliporeSigma, US). The cells were sub-cultured every 2 to 3 days and maintained at 37 °C, 5% (v/v) CO_2 in a humidified incubator.
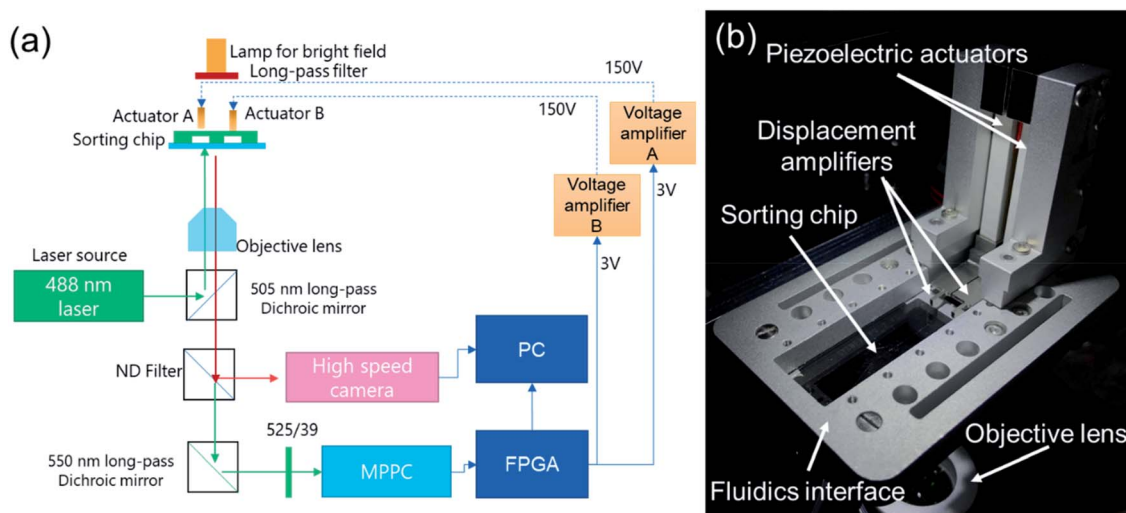
Fig. 4 Overview of the constructed fluorescence–activated cell sorting system. (a) Schematic of the optical detection system. (b) Photograph of the experimental setup.

3.4 Cell viability test

All cells were stained with Hoechst 33342 solution (Dojindo, Japan), while dead cells were stained with 7-AAD viability staining solution (BioLegend, US). A flow cytometer (FACSVerse, BD Biosciences, US) was used to quantify the number of cells after staining. The dead cell ratio was evaluated by means of the ratio of 7-AAD stained cell number to the total cell number. The cell viability was then obtained by subtracting the dead cell ratio from 1.

3.5 Sorting performance evaluation method

Both microparticles and cells were used for performance evaluation. Green fluorescent beads (Fluoro-Max, 15 μm, Thermo Scientific, US) were used as target beads and intentionally spiked into non-target red fluorescent beads (Fluoro-Max, DIAM. 3.2 μm, Thermo Scientific, US) in deionized water at a target frequency of ~0.5%. To investigate the relationship between purity and throughput, total concentration of samples was independently prepared as ~2.3 × 10^5, 6.5 × 10^5, 1.1 × 10^6, 1.7 × 10^6, 3.3 × 10^6 beads per mL. Additionally, green fluorescent beads of different size (Fluoro-Max, DIAM. 5 μm, 10 μm, 15 μm, 25 μm, Thermo Scientific, US) were separately used to study the size dependency of sorting performance, targeting a total concentration of ~2.3 × 10^5 beads per mL. For flow profiling during sorting, green fluorescent beads (Fluoro-Max, 10 μm, Thermo Scientific, US) were encapsulated into uniform ~30 μm water droplets in oil (FC40, RAN Biotechnologies, US) using a commercial droplet generation chip (3200286, Dolomite Microfluidics, UK) at a target frequency of ~0.01%.

MCF-7 cells were stained with carboxyfluorescein diacetate succinimidyl ester (CFSE, Thermo Scientific, US) and spiked into Hoechst 33342 (Dojindo, Japan) stained Jurkat cells in RPMI medium at a target frequency of ~0.5%. Total cell concentration was prepared as ~3 × 10^5 cells per mL.

Quantification before and after sorting was carried out on a flow cytometer, (Accuri C6, BD Biosciences, US), where 50 μL of samples were measured under customized slow flow rate mode. Experiments were repeated three times for each condition. Meanwhile, fluorescence images of samples were taken before and after sorting, using a fluorescence microscope (BZ-X710, Keyence, Japan).

400 μL of mixed beads solution or cell mixture solution was input into the sorting chip at a flow rate of ~40 μL min^{-1}, while the flow rate of the sheath solution was maintained as ~120 μL min^{-1}. Deionized water and RPMI medium are separately used as sheath solutions for the sorting of microparticles and cells. The sampling rate was set as 100 kHz for signal collection, while the threshold for triggering of sorting signals was adjusted to achieve an over 80% yield. The sorting duration to collect target beads was set as 0.2 ms. Both the total sorting time and volume of the collected sample were recorded for performance calculation.

4 Results and discussion

4.1 Calculation of sorting responsiveness using on-chip flow switching

To complete a rapid sorting action, a high operating frequency is demanded in all processes of the as-constructed sorting system, including signal sampling, digital trigger output, voltage amplification, piezoelectric actuation, valving, and recovery of the microchannel. The overall operating frequency is determined by the slowest step of the entire sorting process.

Using the FPGA model, an action of receiving sample signal and outputting the 3 V digital trigger could be finished within microseconds, which qualifies an operation of over 100 kHz.

According to technical specifications, the unloaded resonant frequency (f_0) of the applied piezoelectric actuator is 34 kHz. Applying a load to the actuator will reduce its resonant

frequency. Giving the mass of the piezoelectric actuator (m, 2.14 g), and the mass of the load (M, 12.79 g), the loaded resonant frequency (f_0') may be estimated using the following equation,

$$f_0' = f_0 \sqrt{\frac{m/3}{m/3 + M}} \quad (5)$$

As is known, the fastest displacement of a piezoelectric actuator can occur in 1/3 of the period of its resonant frequency, which indicates a theoretical operating frequency of ~2.6 kHz for this setup. Meanwhile, to achieve a fast response, large peak current is required for charging the piezoelectric actuators. Upon loading of a pulsed voltage, the minimal rise time of voltage on piezoelectric actuators can be determined using the following equation,

$$t \approx C \frac{V_{pp}}{I_{max}} \quad (6)$$

where V_{pp} is peak-to-peak voltage (150 V, in this work), t is minimal rise time until the piezoelectric actuator is fully charged, C is the capacitance of piezoelectric actuator (0.82 μF), and I_{max} is the peak current of the power amplifier (1 A). As a result, the time between t_{tri} and t_{rise} could be easily calculated as 123 μs for our setup. This was confirmed using a commercial oscilloscope. Discharging time after voltage loading for recovery was measured to be the same as the charging time, allowing for an operating frequency of ~4 kHz, which is higher than the theoretical operating frequency.

As passive deformation of PDMS microchannel induced by piezoelectric actuation was used as an on-chip microvalve, as shown in Fig. 1(c), rapid recovery of the same microchannel to its original status after deformation is also required. The recovery speed depends on the natural frequency of the PDMS channel, which could be determined by the following equation,[39]

$$f = \frac{10.21}{2\pi r_0^2} \sqrt{\frac{Eh^2}{12\rho(1-\nu^2)}} \quad (7)$$

where E, ρ, and ν are Young's modulus, density, and Poisson's ratio of the PDMS sheet, respectively. r_0 is the deformation radius of the microchannel. The recovery time of PDMS microchannel was calculated to be ~3.3 μs, which is negligible when compared to the practical operating frequency of piezoelectric actuators. Hence, the valving speed of the microchannel is determined by the theoretical operating frequency of piezoelectric actuators, which is ~2.6 kHz for this setup.

4.2 Profiling of on-chip flow switching

To illustrate the flow profile during a sorting actuation, sequential images were taken before, during, and after sorting, as shown in Fig. 5. Instead of microparticles, water-in-oil droplets with a uniform diameter of 30 μm were input as the sample to enhance light scattering. Moreover, the sample was injected into the microchannel in a bulky way instead of a one-by-one sequential manner. Fig. 5(a) shows an image at a moment before sorting, where the waste channel is open, and
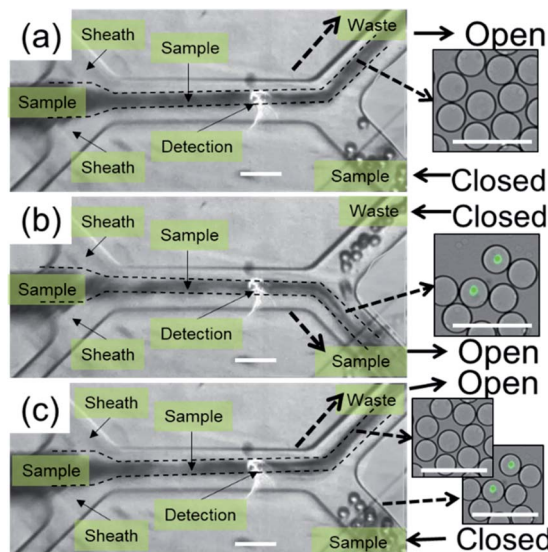

Fig. 5 Sequential images of flow profile at consecutive moments, (a) before sorting, (b) during sorting and (c) after sorting. Images of the sorted droplets were taken under a microscope and provided on the right side of sequential images. Scale bar represents 100 μm in all images.

the sample channel is closed. On detection of a fluorescent signal, the intensity of which is higher than the preset threshold, the sample channel was opened promptly, while the waste channel was closed at the same time, causing fluid at the sorting site flowing into the sample channel, as shown in Fig. 5(b). As a result, target droplets will be guided into the sample channel during the sorting period. After sorting, the sample channel was subsequently closed, while the waste channel was simultaneously opened, setting streams back to the initial status. Due to the bulky sample injection, droplets with green fluorescent beads were only enriched from ~0.008% to ~1%. However, the sorting performance could be improved by lining up droplets and optimizing sorting conditions, in a similar way as we will discuss for sorting of microparticles and cells.

Sequential images of the on-chip sorting of fluorescent microparticles are provided in Fig. 6. Although sample contrast was reduced, flow modulation during a sorting actuation was observed to follow the same manner as shown in Fig. 5. A target fluorescent bead was successfully detected and sorted into the sample channel, as marked in the red dotted circle in Fig. 6(b) and (c). Correspondingly, the following solution without target particles was flowed into the waste channel, as shown in Fig. 6(a) and (d). The fluorescence activated sorting of microparticles is also shown by a video in the ESI, where the positions of microparticles are marked by yellow arrows.†

4.3 Sorting performance of the microfluidic fluorescence-activated sorter

As a qualitative comparison, Fig. 7(a) and (b) show photos of the original sample and sorted sample for a fluorescent microparticles mixture, with 0.66% of 15 μm green target beads. It could
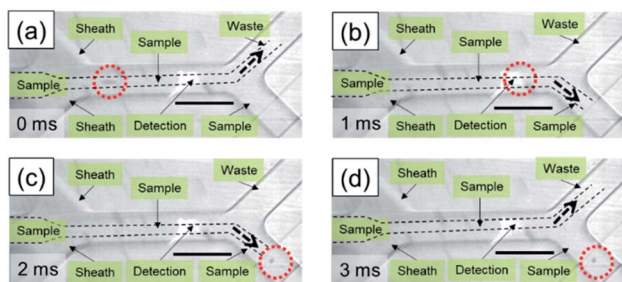
Fig. 6 Sequential images of the on-chip microparticles sorting at consecutive moments, (a) before sorting, (b) on detection, (c) during sorting and (d) after sorting. Scale bar represents 200 μm in all images.

$$Yield = \frac{count\ of\ collected\ target\ beads}{count\ of\ all\ input\ target\ beads} \quad (9)$$

$$Purity = \frac{count\ of\ collected\ target\ beads}{count\ of\ all\ collected\ beads} \quad (10)$$

be observed that the frequency of green fluorescent beads in the sorted sample has been increased significantly from that of the original sample. The enrichment was also confirmed by FCM scatters measured before and after sorting, as shown in Fig. 7(c) and (d).

To quantitatively evaluate the performance of the as-constructed on-chip sorter, FCM results were utilized to calculate throughput, yield, and purity by the following equations,

$$Throughput = \frac{total\ amount\ of\ input\ beads}{total\ costed\ sorting\ time} \quad (8)$$

According to data from three repeated experiments, green fluorescent beads were found to be enriched from 0.66% (±0.02%) to 59.86% (±2.33%), which reveals a 90-fold enrichment for a sorting throughput of 1200 eps. Based on the obtained FCM results, yield (recovery rate) could be optimized to ~98.5%, indicating no obvious sample loss during sorting.

Similar to other microfluidic sorters,[52] trade-offs among throughput, yield, and purity were also observed in this work. In our experiments, settings of the on-chip sort system were optimized to obtain a high yield in favor of purity. However, purity can also be improved in favor of the yield or throughput. Fig. 8 shows the plot of purity as a function of throughput where throughput was adjusted by changing sample concentration. The yield was maintained to be higher than 80% for all these experiments. The purity of the sorted sample is observed to decrease as throughput increases, following the prediction of Poisson distribution. The sampling rate of our data acquisition (DAQ) unit set a limitation on the flow rate of sample delivery.
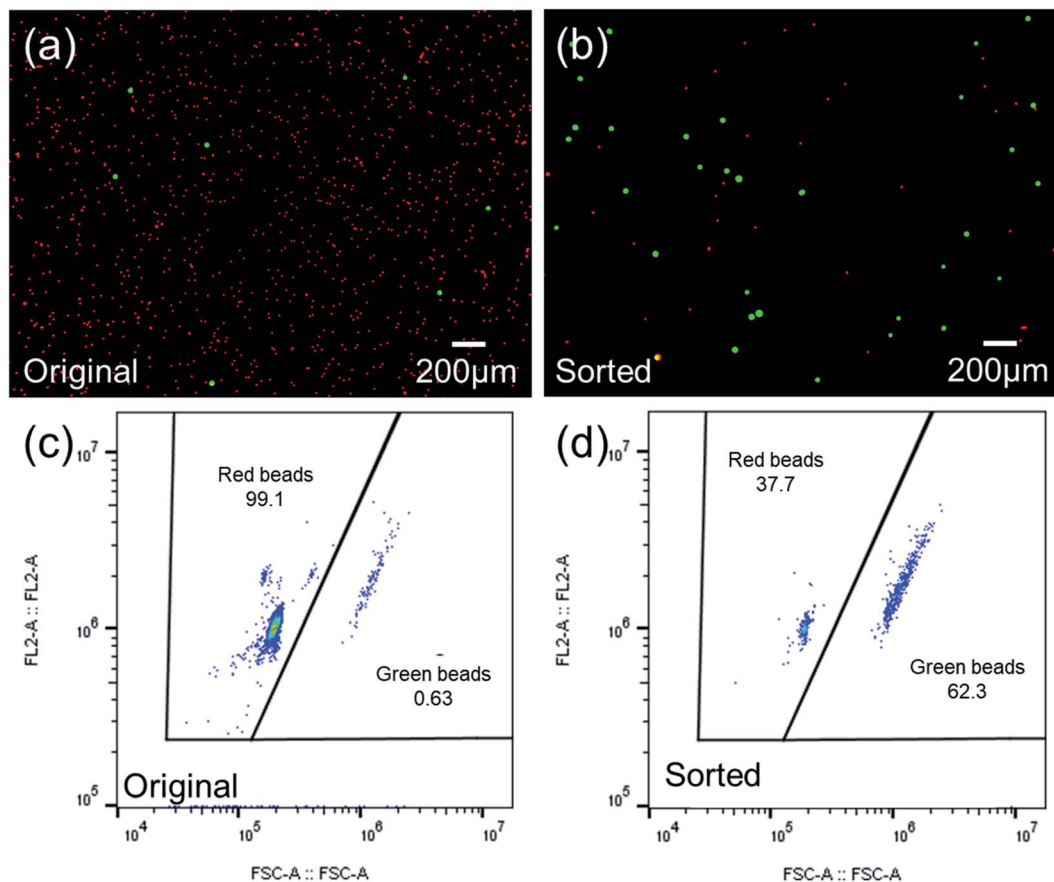
Fig. 7 Frequency comparison between the original sample and sorted sample for 0.66% (±0.02%) green fluorescent beads, (a and b) fluorescent images, (c and d) typical FCM scatters for a sorting throughput of 1200 eps.
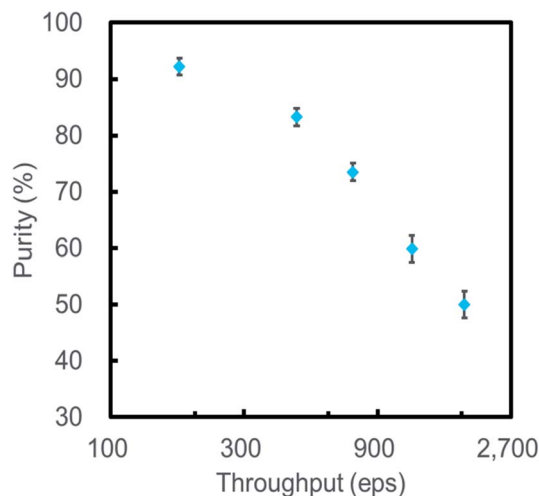
RSC Advances

Paper

Fig. 8 Plot of purity as a function of throughput. (N3, ± 1SD).

Hence, throughput was demonstrated up to ~1800 eps in Fig. 8, resulting in purity between ~92% and ~50%. With an upgraded DAQ unit and a new chip design, a higher purity could be achieved near the theoretical operating frequency, by diluting the input sample, improving the sample flow rate, and reducing flow-switching time.

Another attractive characteristic of the as-demonstrated sorting mechanism is its high versatility in target material properties. Unlike other microfluidic sorting approaches, the flow switching sorting mechanism only allows one downstream microchannel to be open at the same time, guaranteeing a reliable control of flow direction. Hence, regardless of differences in physical properties, as long as the presence of the target could be accurately detected, reliable sorting actuation would be performed. Fig. 9(a)–(d) shows the fluorescent images of the original sample and sorted sample for solutions spiked with target beads of varied sizes (purity of 0.67% ± 0.05% for 5 μm-diameter beads; purity of 0.49% ± 0.08% for 10 μm-diameter beads; purity of 0.57% ± 0.03% for 15 μm-diameter beads; purity of 0.58% ± 0.09% for 25 μm-diameter beads). Significant enrichment was confirmed for all the samples by statistics in Fig. 9(e). This property shows the potential for recovery of precious rare cells without size bias[53,54] and stable sorting of large-volume biological compartments,[55] such as droplets as described in Section 4.2. Although not obvious, the purity is observed to decrease slightly as the target particle diameter decreases. The intensity reduction of signals from small target beads leads to a decrease in the signal-to-noise ratio, which would further reduce the detection resolution. Therefore, a small amount of false sorting actions caused by noise may be responsible for the decrease in purity.

To further demonstrate the sorting performance, fluorescently labeled MCF-7 breast cancer cells were spiked in Jurkat cells in RPMI medium, as shown in Fig. 10(a). The cell mixture was input as the sample for cell sorting experiments. The sorting conditions remained the same as the microparticle sorting experiments. Fig. 10(b) and (c) show fluorescent images of the original cell mixture and sorted sample. Significant enrichment of MCF-7 cells was observed. Typical FCM scatters before and after sorting of the cell mixture are given in Fig. 11(a) and (b). Most of the Jurkat cells are confirmed to be removed after sorting. Statistical results from three repeated experiments show that purity was improved from 0.61% (±0.01%) to 91.01%

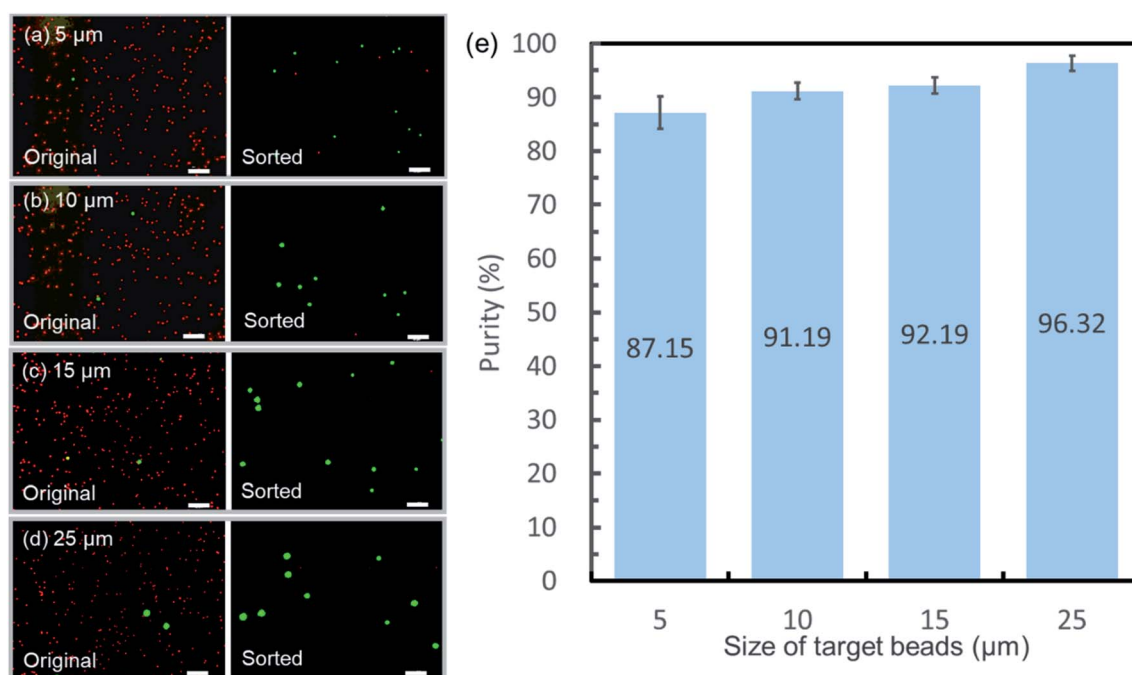Fig. 9 Fluorescent images of the original sample and sorted sample for solutions spiked with varied-size target beads: (a) 5 μm, (b) 10 μm, (c) 15 μm, and (d) 25 μm. (e) The purity of sorted samples (N3, ± 1SD). Scale bar represents 200 μm in all images.

4 T. Weber, B. Wefers, W. Wurst, S. Sander, K. Rajewsky and R. Kühn, *Nat. Biotechnol.*, 2015, **33**, 543–548.

5 M. J. Tomlinson, S. Tomlinson, X. B. Yang and J. Kirkham, *J. Tissue Eng.*, 2013, **4**, 2041731412472690.

6 A. W. Wognum, A. C. Eaves and T. E. Thomas, *Arch. Med. Res.*, 2003, **34**, 461–475.

7 S. Eminli, A. Foudi, M. Stadtfeld, N. Maherali, T. Ahfeldt, G. Mostoslavsky, H. Hock and K. Hochedlinger, *Nat. Genet.*, 2009, **41**, 968.

8 L. Chin, J. N. Andersen and P. A. Futreal, *Nature Medicine*, 2011, **17**, 297–303.

9 Z. Ma, Y. Zhou, D. J. Collins and Y. Ai, *Lab Chip*, 2017, **17**, 3176–3185.

10 J. Guo, X. Huang and Y. Ai, *Anal. Chem.*, 2015, **87**, 6516–6519.

11 R. Gomez-Sjoeberg, A. A. Leyrat, D. M. Pirone, C. S. Chen and S. R. Quake, *Anal. Chem.*, 2007, **79**, 8557–8563.

12 V. Lecault, M. VanInsberghe, S. Sekulovic, D. J. H. F. Knapp, S. Wohrer, W. Bowden, F. Viel, T. McLaughlin, A. Jarandehei and M. Miller, *Nat. Methods*, 2011, **8**, 581.

13 H. Van Phan, M. B. Coşkun, M. Şeşen, G. Pandraud, A. Neild and T. Alan, *Lab Chip*, 2015, **15**, 4206–4216.

14 D. P. Kise, D. Magana, M. J. Reddish and R. B. Dyer, *Lab Chip*, 2014, **14**, 584–591.

15 S. Ma, D. N. Loufakis, Z. Cao, Y. Chang, L. E. K. Achenie and C. Lu, *Lab Chip*, 2014, **14**, 2905–2909.

16 R. Zhang, X. Li, G. Ramaswami, K. S. Smith, G. Turecki, S. B. Montgomery and J. B. Li, *Nat. Methods*, 2014, **11**, 51.

17 J. El-Ali, P. K. Sorger and K. F. Jensen, *Nature*, 2006, **442**, 403–411.

18 D. R. Link, E. Grasland-Mongrain, A. Duri, F. Sarrazin, Z. Cheng, G. Cristobal, M. Marquez and D. A. Weitz, *Angew. Chem., Int. Ed.*, 2006, **45**, 2556–2560.

19 T. Beneyton, F. Coldren, J. C. Baret, A. D. Griffiths and V. Taly, *Analyst*, 2014, **139**, 3314–3323.

20 L. Mazutis, J. Gilbert, W. L. Ung, D. A. Weitz, A. D. Griffiths and J. A. Heyman, *Nat. Protoc.*, 2013, **8**, 870.

21 R. Pethig, *Biomicrofluidics*, 2010, **4**, 1–35.

22 L. Chen and R. B. Fair, *Microfluid. Nanofluid.*, 2015, **19**, 1349–1361.

23 M. Kühnemund, D. Witters, M. Nilsson and J. Lammertyn, *Lab Chip*, 2014, **14**, 2983–2992.

24 B. Watson, J. Friend and L. Yeo, *Sens. Actuators, A*, 2009, **152**, 219–233.

25 S. Li, X. Ding, F. Guo, Y. Chen, M. I. Lapsley, S.-C. S. Lin, L. Wang, J. P. McCoy, C. E. Cameron and T. J. Huang, *Anal. Chem.*, 2013, **85**, 5468–5474.

26 P. Li, Z. Ma, Y. Zhou, D. J. Collins, Z. Wang and Y. Ai, *Anal. Chem.*, 2019, **91**, 9970–9977.

27 Y. Zhou, Z. Ma and Y. Ai, *RSC Adv.*, 2019, **9**, 31186–31195.

28 P. Li, M. Liang, X. Lu, J. J. M. Chow, C. J. A. Ramachandra and Y. Ai, *Anal. Chem.*, 2019, **91**, 15425–15435.

29 L. Schmid, D. A. Weitz and T. Franke, *Lab Chip*, 2014, **14**, 3710–3718.

30 J. Zhang, J. H. Hartman, C. Chen, S. Yang, Q. Li, Z. Tian, P. H. Huang, L. Wang, J. N. Meyer and T. J. Huang, *Lab Chip*, 2020, **20**, 1729–1739.

31 T. Franke, S. Braunmüller, L. Schmid, A. Wixforth and D. A. Weitz, *Lab Chip*, 2010, **10**, 789–794.

32 K. Mutafopulos, P. Spink, C. D. Lofstrom, P. J. Lu, H. Lu, J. C. Sharpe, T. Franke and D. A. Weitz, *Lab Chip*, 2019, **19**, 2435–2443.

33 Z. Ma, D. J. Collins, J. Guo and Y. Ai, *Anal. Chem.*, 2016, **88**, 11844–11851.

34 M. Sivaramakrishnan, R. Kothandan, D. K. Govindarajan, Y. Meganathan and K. Kandaswamy, *Curr. Opin. Biomed. Eng.*, 2020, **13**, 60–68.

35 L. Wu, P. Chen, Y. Dong, X. Feng and B.-F. Liu, *Biomed. Microdevices*, 2013, **15**, 553–560.

36 Z. Cao, F. Chen, N. Bao, H. He, P. Xu, S. Jana, S. Jung, H. Lian and C. Lu, *Lab Chip*, 2013, **13**, 171–178.

37 C. H. Chen, S. H. Cho, F. Tsai, A. Erten and Y. H. Lo, *Biomed. Microdevices*, 2009, **11**, 1223–1231.

38 Z. Cheng, X. Wu, J. Cheng and P. Liu, *Microfluid. Nanofluid.*, 2017, **21**, 9.

39 S. Sakuma, Y. Kasai, T. Hayakawa and F. Arai, *Lab Chip*, 2017, **17**, 2760–2767.

40 Y. Zhao, A. S. Abdelfattah, Y. Zhao, A. Ruangkittisakul, K. Ballanyi, R. E. Campbell and D. J. Harrison, *Integr. Biol.*, 2014, **6**, 714–725.

41 Z. Jiao, X. Huang, N. T. Nguyen and P. Abgrall, *Microfluid. Nanofluidics*, 2008, **5**, 205–214.

42 Y.-F. Yap, S.-H. Tan, N.-T. Nguyen, S. M. S. Murshed, T.-N. Wong and L. Yobas, *J. Phys. D: Appl. Phys.*, 2009, **42**, 65503.

43 M. Robert de Saint Vincent, R. Wunenburger and J.-P. Delville, *Appl. Phys. Lett.*, 2008, **92**, 154105.

44 H. D. Xi, H. Zheng, W. Guo, A. M. Gañán-Calvo, Y. Ai, C. W. Tsao, J. Zhou, W. Li, Y. Huang, N. T. Nguyen and S. H. Tan, *Lab Chip*, 2017, **17**, 751–771.

45 A. Y. Fu, H. P. Chou, C. Spence, F. H. Arnold and S. R. Quake, *Anal. Chem.*, 2002, **74**, 2451–2457.

46 H. Q. Li, D. C. Roberts, J. L. Steyn, K. T. Turner, O. Yaglioglu, N. W. Hagood, S. M. Spearing and M. A. Schmidt, *Sens. Actuators, A*, 2004, **111**, 51–56.

47 I. Fazal and M. C. Elwenspoek, *J. Micromech. Microeng.*, 2007, **17**, 2366–2379.

48 J. M. Park, R. P. Taylor, A. T. Evans, T. R. Brosten, G. F. Nellis, S. A. Klein, J. R. Feller, L. Salerno and Y. B. Gianchandani, *J. Micromech. Microeng.*, 2007, **18**, 15023.

49 D. Zhang, J. Lv, Y. Jiang, H. Chen and J. Fu, *Mechatronics*, 2014, **24**, 511–518.

50 S. Chen, S. Lu, Y. Liu, J. Wang, X. Tian, G. Liu and Z. Yang, *AIP Adv.*, 2016, **6**, 45112.

51 J. Y. Qian, C. W. Hou, X. J. Li and Z. J. Jin, *Actuation mechanism of microvalves: A review*, 2020, vol. 11, pp. 172.

52 N. Nitta, T. Sugimura, A. Isozaki, H. Mikami, K. Hiraki, S. Sakuma, T. Iino, F. Arai, T. Endo, Y. Fujiwaki, H. Fukuzawa, M. Hase, T. Hayakawa, K. Hiramatsu, Y. Hoshino, M. Inaba, T. Ito, H. Karakawa, Y. Kasai, K. Koizumi, S. W. Lee, C. Lei, M. Li, T. Maeno, S. Matsusaka, D. Murakami, A. Nakagawa, Y. Oguchi, M. Oikawa, T. Ota, K. Shiba, H. Shintaku, Y. Shirasaki, K. Suga, Y. Suzuki, N. Suzuki, Y. Tanaka, H. Tezuka,

Paper

RSC Advances

C. Toyokawa, Y. Yalikun, M. Yamada, M. Yamagishi, T. Yamano, A. Yasumoto, Y. Yatomi, M. Yazawa, D. Di Carlo, Y. Hosokawa, S. Uemura, Y. Ozeki and K. Goda, *Cell*, 2018, **175**, 266–276.e13.

53 W. Zhao, Y. Liu, B. D. Jenkins, R. Cheng, B. N. Harris, W. Zhang, J. Xie, J. R. Murrow, J. Hodgson, M. Egan, A. Bankey, P. G. Nikolinakos, H. Y. Ali, K. Meichner, L. A. Newman, M. B. Davis and L. Mao, *Lab Chip*, 2019, **19**, 1860–1876.

54 K. Alix-Panabières and C. Pantel, *Nat. Rev. Cancer*, 2014, **14**, 623–631.

55 A. Isozaki, Y. Nakagawa, M. H. Loo, Y. Shibata, N. Tanaka, D. L. Setyaningrum, J.-W. Park, Y. Shirasaki, H. Mikami, D. Huang, H. Tsoi, C. T. Riche, T. Ota, H. Miwa, Y. Kanda, T. Ito, K. Yamada, O. Iwata, K. Suzuki, S. Ohnuki, Y. Ohya, Y. Kato, T. Hasunuma, S. Matsusaka, M. Yamagishi, M. Yazawa, S. Uemura, K. Nagasawa, H. Watarai, D. Di Carlo and K. Goda, *Sci. Adv.*, 2020, **6**, eaba6712.